Magnetoelectric phase diagrams of orthorhombic $R\mathrm{MnO_3}$ (R=Gd, Tb, and Dy)

T. Kimura and G. Lawes*
Los Alamos National Laboratory, Los Alamos, New Mexico 87545, USA

T. Goto
Department of Applied Physics, University of Tokyo, Tokyo 113-8656, Japan

Y. Tokura
Department of Applied Physics, University of Tokyo, Tokyo 113-8656, Japan
and Superstructure Project, ERATO, Japan Science and Technology Agency, Tsukuba 305-8562, Japan

A. P. Ramirez
Bell Laboratories, Lucent Technologies, 600 Mountain Avenue, Murray Hill, New Jersey 07974, USA
(Received 22 November 2004; revised manuscript received 17 February 2005; published 29 June 2005)

Magnetoelectric phase diagrams have been investigated for rare-earth manganites with orthorhombically distorted perovskite structure, $R\mathrm{MnO_3}$ (R=Gd, Tb, and Dy). A variety of magnetic and electric phases emerge with varying R-site ion, temperature, and magnetic field in these systems. The magnetoelectric phase diagram varies sensitively with the direction of a magnetic field relative to the crystallographic axes. Although the ground state of $\mathrm{GdMnO_3}$ with the largest ionic radius of $R(r_R)$ is not ferroelectric in zero magnetic fields (H=0), a ferroelectric phase with electric polarization (P) along the a axis appears by applying $H(>\sim 1$ T) along the b axis. Both $\mathrm{TbMnO_3}$ and $\mathrm{DyMnO_3}$ show a ferroelectric order with P along the c axis even at H=0 below a lock-in transition temperature where nonzero wave vectors for magnetic and lattice modulations become nearly constant. These systems also exhibit a flop of the ferroelectric polarization ($P\|c$ to $P\|a$) when H is applied along the a or b axis. By contrast, the application of H above $\sim$10 T along the c axis completely suppresses the ferroelectricity in $\mathrm{TbMnO_3}$. Possible origins of the observed evolution of magnetoelectric phases are discussed in consideration of magnetism and lattice distortion in the perovskite rare-earth manganites.

DOI: 10.1103/PhysRevB.71.224425 PACS number(s): 75.47.Lx, 75.80.+q, 64.70.Rh, 77.80.−e

I. INTRODUCTION

The study of magnetic ferroelectrics where both magnetic and ferroelectric orders coexist attracted a great deal of interest in 1960s and 1970s,[1] as the coupling between the magnetization and electric polarization can provide an additional degree of freedom in "magnetoelectric" device design.[2] In the past several years, there has been a revival of interest in magnetoelectric research of magnetic ferroelectrics[3–7] that are recently referred to also as *magnetoelectric multiferroics*,[8,9] motivated in part by extensive studies on exploring for spin-electronics materials. Although several magnetoelectric multiferroics have been identified to date,[1,2] there have been no practical applications of magnetoelectric phenomena due mainly to the small magnitude of the magnetoelectric or magnetocapacitive effects.[10] In most of the earlier magnetoelectric multiferroics listed in Ref. 1, the temperature scale for ferroelectric order is much larger than for magnetic order. This leads to only weak coupling between magnetism and ferroelectricity in these systems.

More recently, gigantic magnetoelectric and magnetocapacitive effects have been found in certain rare-earth manganites having antiferromagnetic (AF) orders with long wavelengths as compared to their chemical unit cell.[11–19] These interactions provide an approach to engineering the couplings between magnetism and ferroelectricity. Recent theoretical and experimental studies of a series of rare-earth manganites with orthorhombically distorted perovskite structure ($R\mathrm{MnO_3}$ where R is a trivalent rare-earth ion) revealed that the ferroelectricity originates from competing magnetic interactions which produce a long-wavelength AF spin order and accordingly lattice modulations with nonzero wave vector through magnetoelastic coupling.[20] This coupling between magnetic order and lattice distortions which produces ferroelectricity gives rise to strong magnetoelectric coupling and resultant gigantic magnetoelectric and magnetocapacitive effects.

In this paper, we provide an overview of the magnetoelectric phase diagrams of the orthorhombic rare-earth manganites, $R\mathrm{MnO_3}$ (R=Gd, Tb, and Dy), which we determined from measurements of the magnetization, dielectric constant, and electric polarization in external magnetic fields. In $R\mathrm{MnO_3}$, a decreasing of ionic radius of the $R(r_R)$ enhances the competition in magnetic interactions, i.e., ferromagnetic (FM) between nearest-neighboring Mn sites and AF between next-nearest-neighboring sites.[20] Figure 1 shows the magnetic phase diagram of $R\mathrm{MnO_3}$ as a function of r_R. (Here, we take r_R for $^{\mathrm{IX}}R^{3+}$ ion from Ref. 21). Around R=Gd, Tb, and Dy, the competing interactions give rise to a long wavelength AF order, which produces ferroelectricity in these manganites through magnetoelastically induced lattice modulations.[12] The present systematic study of magnetoelectric phenomena provides a coherent picture of how magnetic

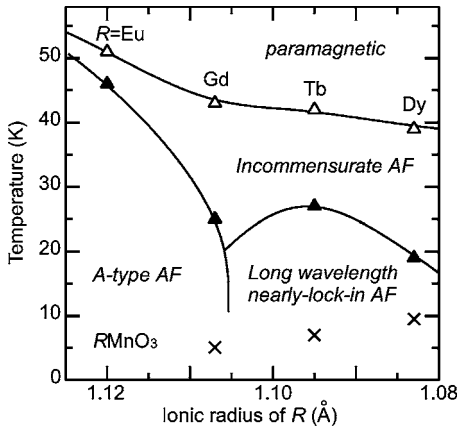

FIG. 1. Magnetic phase diagram for $R\mathrm{MnO_3}$ as a function of ionic radius of R. Open and closed triangles denote the Néel temperature for Mn moments $T_N(\mathrm{Mn})$ and the lock-in transition temperature T_{lock}, respectively. Crosses denote the Néel temperature for R moments $T_N(R)$. These magnetic ordered phases can be characterized by propagation vectors $(0,k_{\mathrm{Mn}},1)$ where k_{Mn} is 0 at the A-type AF phase, is temperature dependent between 0 and $\frac{1}{2}$ for the incommensurate AF phase, and is locked at values between 0 and $\frac{1}{2}$ for the long wavelength nearly-lock-in AF phase.

fields affect dielectric and ferroelectric properties in certain magnetoelectric multiferroics.

II. EXPERIMENTAL PROCEDURES

Crystals of orthorhombic $R\mathrm{MnO_3}$ (R=Gd, Tb, and Dy) were grown by the floating zone method at a feed rate of 10 mm/h. $\mathrm{GdMnO_3}$ and $\mathrm{TbMnO_3}$ crystals were grown in a flow of 6N-purity Ar gas. For $\mathrm{DyMnO_3}$, growths in an Ar atmosphere produced not the perovskite like but the hexagonal phase. Therefore, we performed the growth of $\mathrm{DyMnO_3}$ in air as reported previously,[22] or in $\sim$10 atm $\mathrm{O_2}$ gas. We measured powder x-ray diffraction patterns of the obtained crystals at room temperature, and confirmed that all the samples used for magnetic and electric measurements have the *Pbnm* orthorhombic structure. The crystals were oriented using Laue x-ray diffraction patterns, and cut into thin plates with the widest faces perpendicular to the crystallographic principal axes (typical dimension $\sim 2\times 2\times 1$ mm^3). The magnetization was measured using commercial magnetometers. For the measurements of the dielectric constant ε and electric polarization P, silver electrodes were vacuum deposited onto the widest faces, and were baked in a flow of Ar at 400 °C for about 2 h. We measured ε at 10 kHz using an LCR meter. Some of measurements in magnetic fields above 9 T were performed at National High Magnetic Field Laboratory in Los Alamos National Laboratory. To obtain the temperature T (magnetic field H) dependence of P, the pyroelectric (magnetoelectric) current was measured with an electrometer while sweeping T at a rate of $\sim$5 K/min (sweeping H at a rate of 0.72–1.2 T/min). These current measurements were performed after poling the crystals ($\sim$200 V/mm) while cooling from a temperature above the Néel temperature for Mn moments $[T_{\mathrm{N}}(\mathrm{Mn})]$. Before measurements, the poling electric field was removed (except for one of measurements shown in Fig. 14). P was obtained by integrating the pyroelectric or magnetoelectric current as a function of time.

III. RESULTS

A. $\mathrm{TbMnO_3}$

First, we review the magnetic, structural, and ferroelectric properties of $\mathrm{TbMnO_3}$ in the absence of external magnetic fields. The Mn moments in $\mathrm{TbMnO_3}$ undergo an AF transition at $T_N(\mathrm{Mn})\sim 41$ K. In a model proposed for the magnetic structure,[23] the Mn moments are aligned along the b axis and show sinusoidal order with a propagation wave vector $(0,k_{\mathrm{Mn}},1)$ in the *Pbnm* orthorhombic unit cell. The $k_{\mathrm{Mn}}(\sim 0.29)$ is incommensurate at $T_N(\mathrm{Mn})$ and decreases with decreasing T, and becoming nearly locked-in at $k_{\mathrm{Mn}}\sim 0.28$ below $T_{\mathrm{lock}}\sim 28$ K. A recent neutron diffraction measurement[24] revealed that weak satellite reflections associated with k_{Mn} exist in Brillouin zones of C-type $(h+k=2p+1, l=2p)$ and F-type $(h+k=2p, l=2p)$ below $T_N(\mathrm{Mn})$ in addition to those of A-type $(h+k=2p, l=2p+1)$ and G-type $(h+k=2p+1, l=2p+1)$ reported previously.[23] Although all the components emerge below $T_N(\mathrm{Mn})$, for temperatures between $T_N(\mathrm{Mn})$ and T_{lock} only the A-type component is evident. The G-, C-, and F-type components are significantly enhanced below T_{lock}. In addition, magnetic reflections at $(0,k_{\mathrm{Mn}},0)$ have been observed below T_{lock}. These results by Kajimoto and co-workers[24] suggest the existence of multiple magnetic phases or a complex noncollinear magnetic order (e.g., spiral) below T_{lock}. Together with the magnetic ordering, $\mathrm{TbMnO_3}$ shows an incommensurate lattice modulation below $T_N(\mathrm{Mn})$.[20] This lattice modulation with wave number $k_l(=2k_{\mathrm{Mn}})$ can be regarded as a second harmonic of the sinusoidal AF structure, and below $T_{\mathrm{lock}}\sim 28$ K k_l is also locked in accordance with the AF lock-in transition. In $\mathrm{TbMnO_3}$, ferroelectric order with spontaneous polarization along the c axis develops at $T_{\mathrm{lock}}(=T_C)$ where a sharp peak is observed in ε measured along the c axis.[11] Upon further decreasing T below $T_N(\mathrm{Tb})\sim 7$ K, the magnetic moments of Tb show quasi-long-range ordering with a different propagation vector $(0,\sim 0.42,1)$ from that of Mn moments.[23,24] Although a small anomaly is observed at $T_N(\mathrm{Tb})$ in the temperature dependence of ε and P,[12] the direction of P was not changed by the magnetic ordering of the Tb moments.

In the previous paper,[11] we discussed the effects of magnetic fields on ε and P only for H along the b axis, and magnetoelectric phase diagram only for the $H\|b$ configuration. In the following we present a complete set of data. Figure 2 displays the temperature profiles of ε along the a, b, and c axes in a range of magnetic fields (0–9 T) parallel to the a, b, and c axes for $\mathrm{TbMnO_3}$. A corresponding set of P data is shown in Fig. 3. Regardless of the direction of H, the dielectric constant along the b axis (ε_b) is almost independent of H [Figs. 2(d), 2(e), and 2(f)], and no electric polarization along the b axis (P_b) is ever induced by the application of H. [Tiny anomalies observed in $\varepsilon_b(P_b)$ may be caused

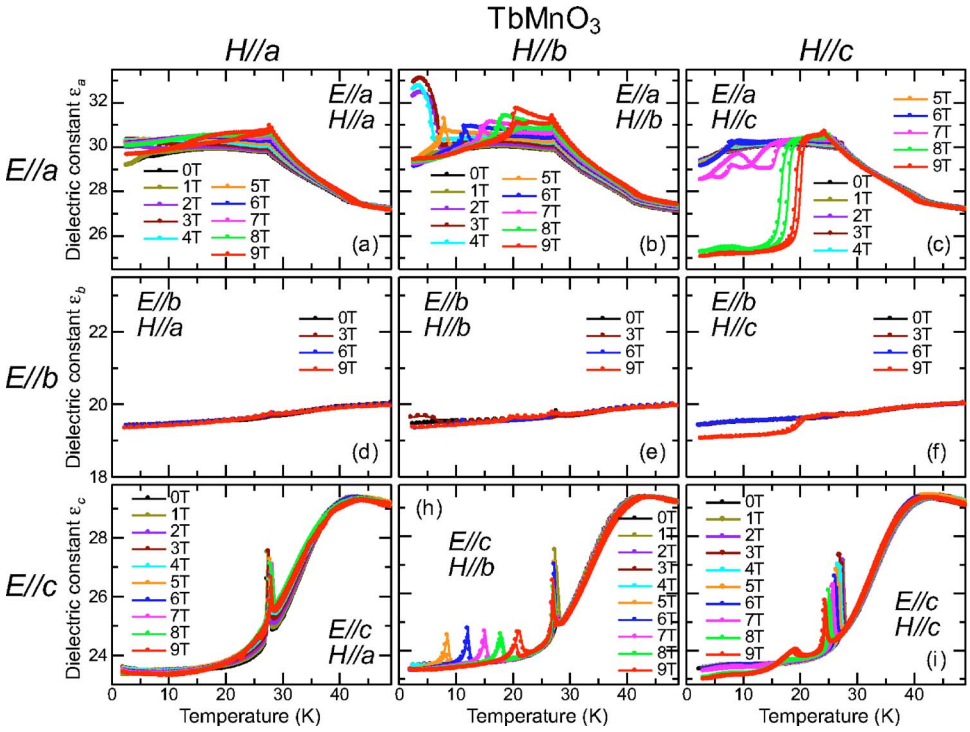

FIG. 2. (Color online) Temperature profiles of dielectric constant along the a, b, and c axes at various magnetic fields (up to 9 T) along the a, b, and c axes for $TbMnO_3$ crystals.

by the components of ε_a or ε_c (P_a or P_c) due to small misalignment of sample axes.] By contrast, ε_a, ε_c, P_a, and P_c are strong functions of H.

When H is applied along the a axis (H_a), ε_a and ε_c increase slightly around T_{lock} [see Figs. 2(a), 2(g), 3(a), and 3(g)]. However, the dielectric anomalies just at T_{lock} (kink in ε_a or sharp peak in ε_c) are almost independent of H_a. Indeed, the onset temperature for the ferroelectric transition T_C shows minimal H dependence, as seen in Fig. 3(g). The P data displayed in Figs. 3(a), 3(d), and 3(g) indicate that the ferroelectricity having a spontaneous polarization along the c axis is robust against H_a up to 9 T, although some magnetic-field effects are observed in magnitude of P_c.

For H applied along the b axis (H_b), more remarkable changes are observed in ε_a, ε_c, P_a, and P_c. The results of this configuration have already been reported in the previous report.[11] We briefly summarize the main features below. Although the sharp peak at T_{lock} in ε_c is not sensitive to the application of H_b, another peak feature appears in ε_c at a temperature (T_{flop}) below T_{lock} above 5 T [Fig. 2(h)]. T_{flop}

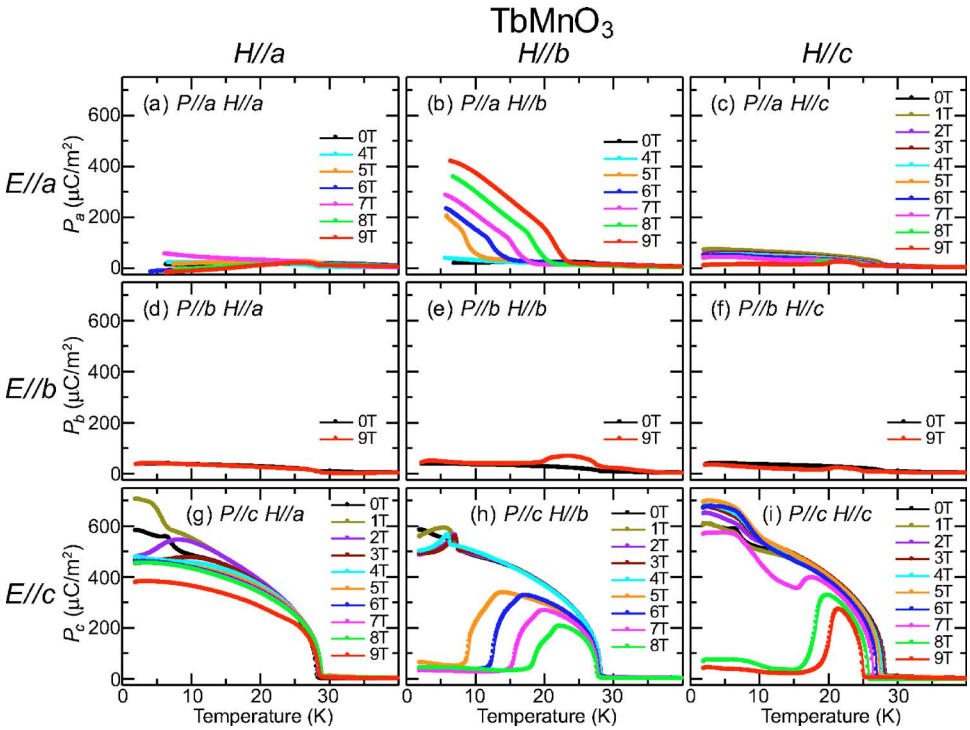

FIG. 3. (Color online) Temperature profiles of electric polarization along the a, b, and c axes at various magnetic fields (up to 9 T) along the a, b, and c axes for $TbMnO_3$ crystals.

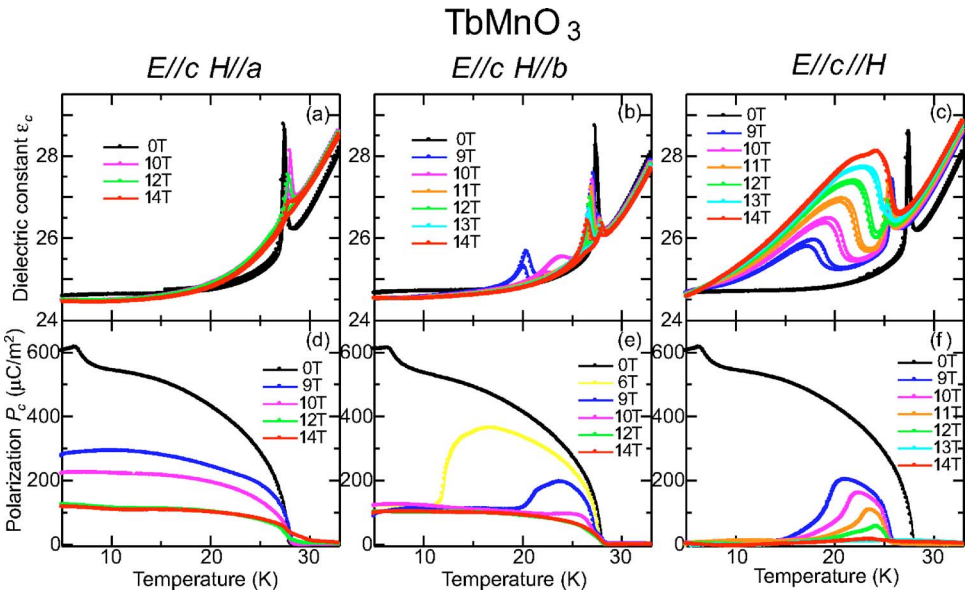

FIG. 4. (Color online) Temperature profiles of (a)–(c) dielectric constant and (d)–(e) electric polarization along the *c* axis at high magnetic fields (9–14 T) along the *a*, *b*, and *c* axes for $TbMnO_3$ crystals.

increases with increasing H_b. ε_a also exhibits a dielectric anomaly at T_{flop} [Fig. 2(b)]. The dielectric anomalies at T_{flop} are attributed to a magnetic-field-induced electric polarization flop, where the ferroelectric polarization vector is switched from pointing along the *c* to the *a* axis by the application of H_b [see Figs. 3(b) and 3(h)]. It is also worth mentioning that ε_a shows a sharp increase below ~7 K at H_b=2~4 T [Fig. 2(b)], which may be related to the change of ordeing structure of the Tb moments.

Applying *H* along the *c* axis (H_c) considerably decreases T_{lock} (~25 K at 9 T), as seen in Figs. 2(i) and 3(i). Such a large shift in T_{lock} is not observed when *H* is applied along the *a* or *b* axis. One of the most striking *H* effects appears in ε_a above ~8 T. As highlighted in Fig. 2(c), ε_a shows a steep drop at a temperature T_{C2} (e.g., T_{C2}~17 K at 8 T) below T_{lock}, while ε_c exhibits a small peak structure at T_{C2} [Fig. 2(i)]. T_{C2} tends to increase with increasing H_c. Corresponding to these dielectric anomalies, P_c also varies with H_c above ~8 T. As shown in Fig. 3(i), the spontaneous polarization along the *c* axis is rapidly suppressed above ~8 T, and almost vanishes below T_{C2}. Although the suppression of P_c by H_c is similar to that produced by an application of H_b [compare Fig. 3(i) and Fig. 3(h)], the behavior of P_a is completely different between the applied field directions, H_b [Fig. 3(b)] and H_c [Fig. 3(c)]. No spontaneous polarization develops along the *a* axis by applying H_c, as seen in Fig. 3(c). These results indicate that the system becomes *not* ferroelectric, i.e., paraelectric or antiferroelectric, below T_{C2} by applying H_c above ~8 T.

We were also interested in exploring the dielectric and ferroelectric features at higher magnetic fields. In Figs. 4 and 5, we display the temperature profiles of ε and *P* along the *c* and *a* axes at magnetic fields up to 14 T.[25] With the application of sufficiently large *H* along the *a* axis, the peak structure at T_{lock} in ε_c is suppressed [Fig. 4(a)], whereas a pronounced peak structure grows at T_{lock} in ε_a [Fig. 5(a)]. This conversion of peak features at T_{lock} from ε_c to ε_a is ascribed to switching *P* from the *c* axis to the *a* axis, as illustrated in

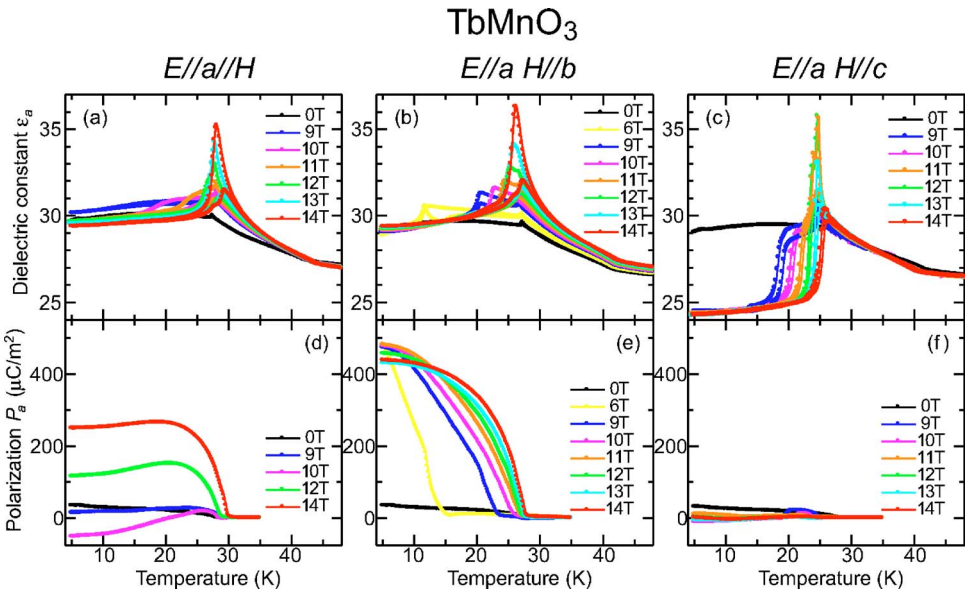

FIG. 5. (Color online) Temperature profiles of (a)–(c) dielectric constant and (d)–(e) electric polarization along the *a* axis at high magnetic fields (9–14 T) along the *a*, *b*, and *c* axes for $TbMnO_3$ crystals.

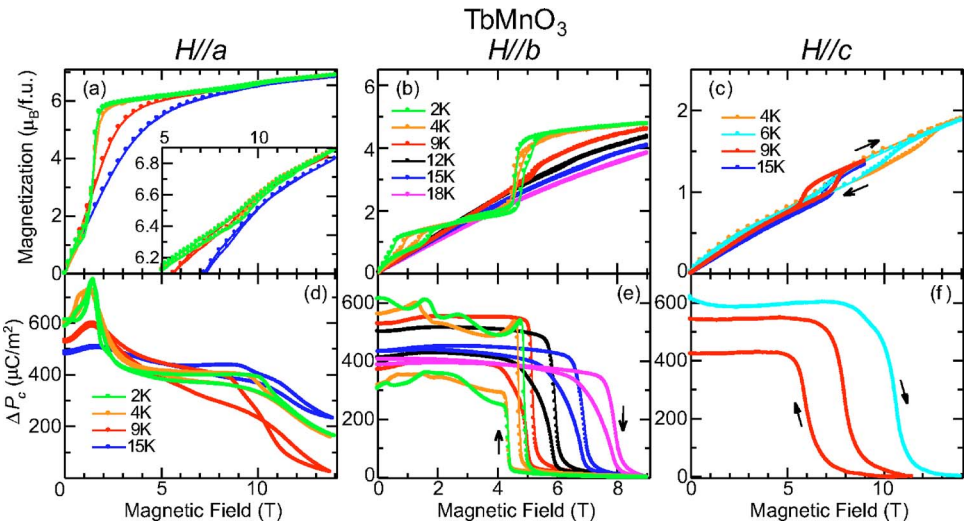

FIG. 6. (Color online) (a)–(c) magnetization and (d)–(f) magnetic-field-induced change in electric polarization along the c axis for $TbMnO_3$ crystals as a function of an external magnetic fields parallel to the a, b, and c axes at fixed temperatures. The inset of (a) shows a magnified view at high H region.

Figs. 4(d) and 5(d).[26] A similar magnetic-field-induced polarization flop from the c axis to the a axis is also observed with a large H_b. Thus, both the applications of H_a and H_b cause the conversion of the direction of P to switch from the c to the a axis.

The effect of a high H along the c axis is distinct from along the a and b axes. The dielectric anomaly in ε_c observed at T_{C2} becomes more evident with increasing H above 9 T [Fig. 4(c)], and the T_{C2} increases monotonically with H. Intriguingly, ε shows remarkable changes below T_{C2} (enhancement of ε_c [Fig. 4(c)] and suppression of ε_a [Fig. 5(c)]). No similar features were observed for H applied along the a and b axes. Another remarkable feature is that ε_a is enormously enhanced when T_{C2} merges into T_{lock} at ~25 K and ~12 T. As clearly seen in the P data [Figs. 4(f) and 5(f)], the polarization almost vanishes for all crystallographic directions and for all temperatures with H above 13 T. We conclude that $TbMnO_3$ becomes *not* ferroelectric by applying sufficiently large H_c.

To explore the relationship between magnetism and these observed dielectric and ferroelectric properties, we measured the isothermal magnetization (M) and polarization as a function of magnetic fields at selected temperatures. As displayed in Figs. 6(a)–6(c), single or double metamagnetic transitions can be seen in M–H curves at 2 or 4 K, depending on the orientation of H. With the application of H_a, double metamagnetic transition has been observed. The first transition shows a distinct jump of M at ~1.7 T [the main panel of Fig. 6(a)], and the second one only exhibits a small change in M at ~10 T [the inset of Fig. 6(a)]. The application of H_b also gives rise to double transitions around ~1 and ~4.5 T [Fig. 6(b)]. The enhancement of ε_a, as observed at H_b=2–4 T below 7 K, occurs in the intermediate phase between the two metamagnetic transitions. With increasing T, the steps in the M–H curves become indistinct. Applying H_c causes a single metamagnetic transition above 5 T, as shown in Fig. 6(c). This metamagnetic transition in H_c is accompanied by a large field hysteresis at low temperatures, and the increase of M at the transition is ~0.2 μ_B/f.u. We will discuss the origin of the metamagnetic transitions later. Comparing the M–H curves with the P–H curves in Fig. 6, it is clear that the metamagnetic transitions give rise to the large changes in P. These results clearly demonstrate the strong interplay between magnetism and ferroelectricity in $TbMnO_3$.

To summarize our experimental results on the dielectric and ferroelectric properties of $TbMnO_3$, we show the magnetoelectric phase diagrams for directions of magnetic fields along the a, b, and c axes in Figs. 7(a), 7(b), and 7(c), respectively. A possible mechanism of the magnetic-field effect on dielectric and ferroelectric properties will be discussed later in more detail.

B. $DyMnO_3$

The magnetic, structural, and ferroelectric properties of $DyMnO_3$ are similar to those of $TbMnO_3$. $DyMnO_3$ also shows an incommensurate crystallographic superstructure below T_N(Mn) ~ 39 K corresponding to sinusoidal AF ordering of the Mn moments.[20] The wave number k_l for the superstructure with a propagation vector $(0,k_l,0)$ is ~0.72 at T_N(Mn), increases with decreasing T, and becomes nearly constant ($k_l \sim 0.77$) below $T_{\text{lock}} \sim 18$ K. By analogy with $TbMnO_3$, the superstructure in $DyMnO_3$ can also be ascribed to a magnetoelastically induced lattice modulation. At T_{lock}($=T_C$), ferroelectric order develops with a spontaneous polarization along the b axis.[12] Anomalies in ε and P has also been observed around $T_N(\text{Dy}) < 10$ K.[12]

In Figs. 8 and 9 we show temperature profiles of ε and P of $DyMnO_3$ along the a and c axes in a range of magnetic fields (0–9 T) parallel to the a, b, and c axes. No substantial T and H dependences were observed in ε_b and P_b, except for small contributions from other directions due to sample misalignment. In $TbMnO_3$, a suppression of P_c was observed at $H > 7$ T for H applied along the c axis, [Fig. 3(i)]. In $DyMnO_3$, however, P_c does not vanish up to H_c=9 T although slight suppressions of T_C and P_c are observed with increasing H_c [Fig. 9(f)]. The application of H_a and H_b causes the ferroelectric polarization vector to switch from the c to the a axis [Figs. 9(a), 9(b), 9(d), and 9(e)], as observed in $TbMnO_3$. In these two configurations, the magnetic-field effect on the ferroelectric properties in $DyMnO_3$ is similar to $TbMnO_3$. It should be noted that ε_a is drastically enhanced

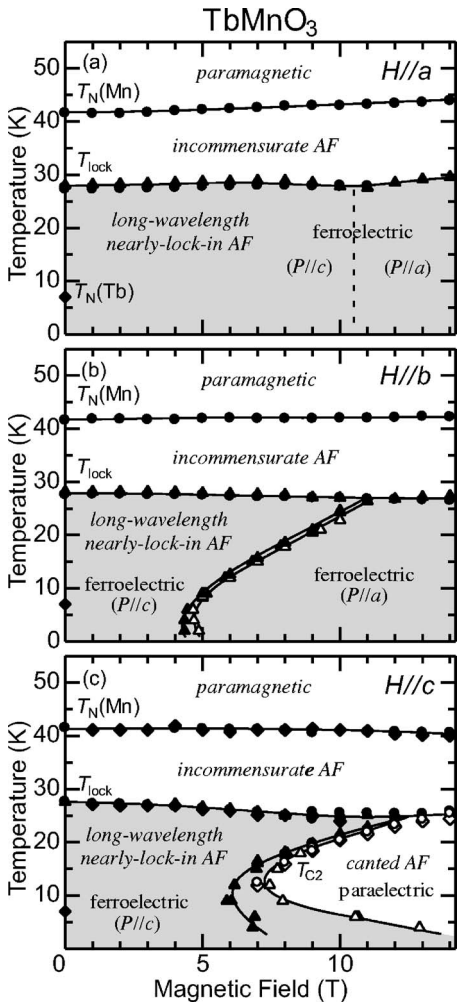

FIG. 7. Magnetoelectric phase diagram of $TbMnO_3$ with magnetic fields along the (a) *a*, (b) *b*, and (c) *c* axes. Circles, triangles, and diamonds represent the data obtained by measurements of dielectric constant, pyroelectric (or magnetoelectric) current, and magnetization, respectively. Open and closed symbols denote the data obtained with decreasing temperature (or increasing a magnetic field) and increasing temperature (or decreasing a magnetic field), respectively. Gray regions indicate ferroelectric phases.

around T_{flop} in magnetic fields along the *a* and *b* axes. By the applying H_b, in particular, the maximum value of ε_a almost reaches ~200 around the tricritical point (~19 K, ~5 T) at which the paraelectric incommensutate AF, the ferroelectric ($P \| c$), and the ferroelectric ($P \| a$) phases meet with each other [Fig. 8(b)]. Consistent with the large value of ε_a, P_a in H_b is larger (~2500 $\mu C/m^2$) at low *T* than what we measured in $TbMnO_3$, as seen in Fig. 9(b). Figure 10 displays ε_a and P_a as a function of H_b, which indicates that a gigantic magnetocapacitive effect [Fig. 10(a)] is associated with the magnetic-field induced polarization flop phenomenon [Fig. 10(b)] where large P_a is induced by relatively low *H* (~2500 $\mu C/m^2$ at 2 K below 2 T).

Observation of hysteresis loop in *P–E* curve is generally taken as a measure of the degree of ferroelectricity. Hence, it is interesting to measure and compare the *P–E* curves in magnetic fields below and above magnetic-field-induced polarization flop. Figure 11 shows the 4.2 K *P–E* curves obtained at 0 and 6 T. Here, magnetic fields were applied along the *b* axis while electric fields were parallel to the *a* axis. No hysteresis loop was observed at 0 T (red line in Fig. 11). However, a clear hysteresis loop characteristic of ferroelectrics was observed in a magnetic field of 6 T. The results are essentially consistent with those obtained by pyroelectric current measurements which revealed that the ferroelectric polarization vector switch from the *c* to the *a* axis by applying H_b.[27]

To summarize the magnetic-field effect on the ferroelectric properties in $DyMnO_3$, we display the magnetoelectric phase diagrams of $DyMnO_3$ for the directions of *H* along the *a*, *b*, and *c* axes in Figs. 12(a), 12(b), and 12(c), respectively. For *H* applied along the *a* and *b* axes, the essential features of the phase diagrams are almost identical with those in $TbMnO_3$. Namely, *H* switches the ferroelectric polarization vectors from the *c* to the *a* axis. However, the magnitude of *H* for the transitions is smaller in $DyMnO_3$ than that in $TbMnO_3$. [Compare Figs. 7(a), 7(b), 12(a), and 12(b).] With $H \| c$, we did not observe any electric phase transitions up to 9 T. We also measured magnetization up to 14 T, but no metamagnetic transition was observed in the configuration with $H \| c$. That is distinct from the case of $TbMnO_3$. A possible origin of the difference will be discussed later.

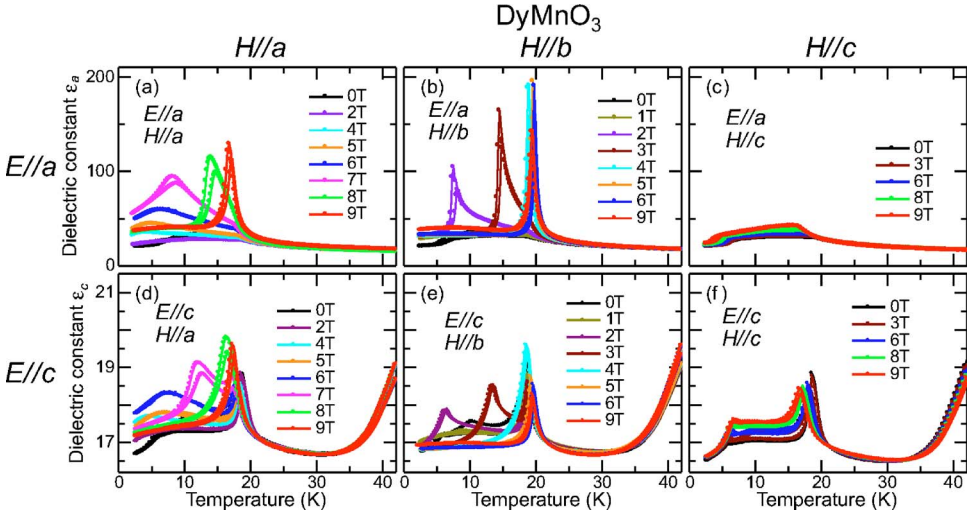

FIG. 8. (Color online) Temperature profiles of dielectric constant along the *a* and *c* axes at various magnetic fields (up to 9 T) along the *a*, *b*, and *c* axes for $DyMnO_3$ crystals.

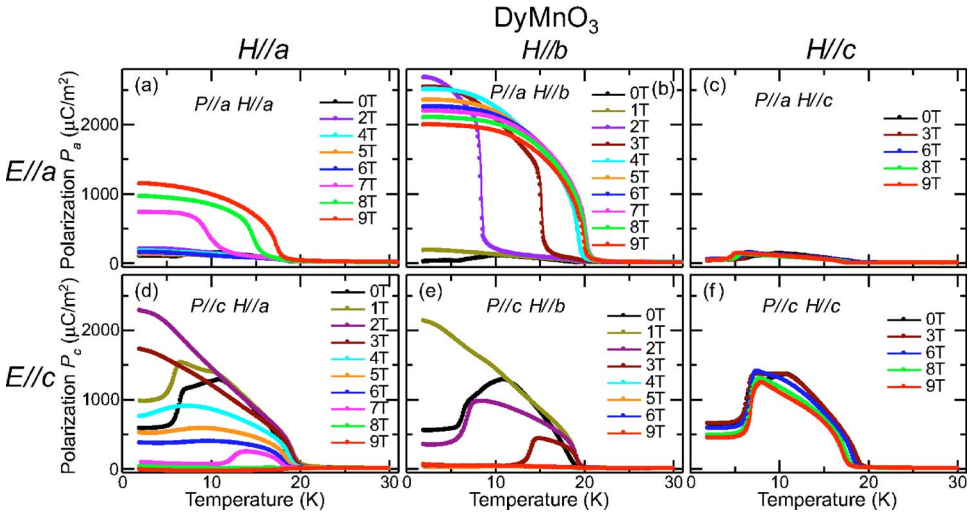

FIG. 9. (Color online) Temperature profiles of electric polarization along the a and c axes at various magnetic fields (up to 9 T) along the a, b, and c axes for $DyMnO_3$ crystals.

C. $GdMnO_3$

$GdMnO_3$ also exhibits a lattice modulation characterized by a propagation vector $(0,k_l,0)$ below $T_N(\mathrm{Mn})\sim 43$ K. The k_l is ~ 0.48 at $T_N(\mathrm{Mn})$, which decreases with decreasing T, then abruptly jumps from ~ 0.39 to 0 at $T_{\mathrm{lock}}\sim 23$ K. This means that the long wavelength modulated structure vanishes below T_{lock}. The lattice modulation between $T_N(\mathrm{Mn})$ and T_{lock} suggests that there may be a modulated spin structure with a propagation vector $(0,k_{\mathrm{Mn}},1)[2k_{\mathrm{Mn}}=k_l]$ in this temperature range, as we found in $TbMnO_3$ and $DyMnO_3$. However, the disappearance of the lattice modulation below T_{lock} implies that the long wavelength modulated spin structure is transformed to another structure in $GdMnO_3$. While we have no specific information regarding the spin structures of $GdMnO_3$, we propose that the sinusoidal AF structure $(\sim 0.2<k_{\mathrm{Mn}}<\sim 0.24)$ above T_{lock} changes into A-type AF order $(k_{\mathrm{Mn}}=0)$ below T_{lock}, motivated by the known magnetic phase diagram for $RMnO_3$.[20] In addition, a recent magnetization study of $GdMnO_3$ also indicates the existence of A-type AF order on Mn sites below T_{lock}.[28] $GdMnO_3$ may not be ferroelectric in the absence of a nonzero wave vector lattice modulation below T_{lock}. Concerning the ordering of Gd moments, Hemberger and co-workers[28] proposed that long-range order of Gd moments evolves below $T_N(\mathrm{Gd})\sim 6.5$ K, yielding a canting of the Gd moments with a FM component antiparallel to the FM moment of the canted Mn spins. The ac-susceptibility data of our $GdMnO_3$ crystal exhibit a peak at ~ 5.1 K (not shown), suggesting $T_N(\mathrm{Gd})\sim 5.1$ K (for temperature increasing run). The location of $GdMnO_3$ in the magnetic phase diagram is in the immediate vicinity of the phase boundary between A-type and long-wavelength AF phases (see Fig. 1). This may make the ferroelectric properties of the system complicated.

In Fig. 13, we plot ε along the a and c axes as a function of T at fixed H applied along the a, b, and c axes. At $H=0,\varepsilon_a$ shows a steep increase at $T_N(\mathrm{Mn})$ toward T_{lock}, followed by a sudden drop at T_{lock}. Upon further decreasing T, another dielectric anomaly is observed in ε_a around $T_N(\mathrm{Gd})$. At T_{lock}, we also observe a sudden increase of ε_c. These dielectric anomalies around T_{lock} and $T_N(\mathrm{Gd})$ accompanies a remarkable thermal hysteresis. As shown in Figs. 13(a) and

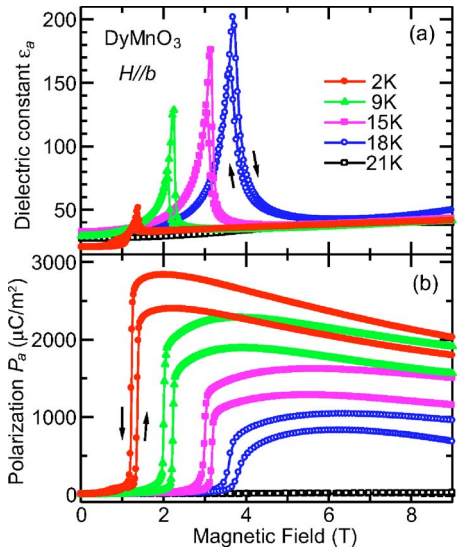

FIG. 10. (Color online) Magnetic-field-induced change in (a) dielectric constant and (b) electric polarization along the a axis at selected temperatures for a $DyMnO_3$ crystal. Magnetic fields are applied along the b axis.

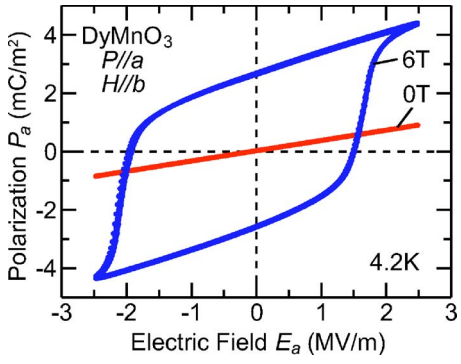

FIG. 11. (Color online) P–E curves obtained at magnetic fields of 0 T (red) and 6 T (blue) for a $DyMnO_3$ crystal. The measurements were done at 4.2 K and 100 Hz. Magnetic and electric fields are applied along the b and a axes, respectively.

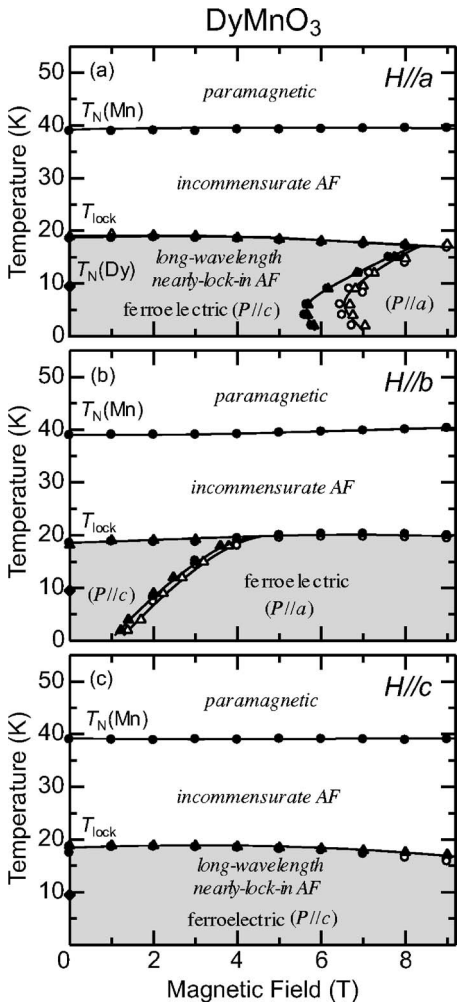

FIG. 12. Magnetoelectric phase diagram of $DyMnO_3$ with magnetic field along the *a* (a), *b* (b), and *c* (c) axes. Circles, triangles, and diamonds represent the data obtained by mea- surements of dielectric constant, pyroelectric (or magnetoelectric) current, and magnetization, respectively. Open and closed symbols denote the data obtained with decreasing temperature (or increasing a magnetic field) and increasing temperature (or decreasing a magnetic field), respectively. Gray regions indicate ferroelectric phases.

13(d), applying H_a shifts the dielectric anomaly at T_{lock} toward higher T and suppresses the anomaly around T_N(Gd). The application of H_b also slightly increases T_{lock} [Figs. 13(b) and 12(e)]. It is also worth noting that the anomaly in ε_a around T_N(Gd) changes its character by applying H_b, although a steep increase of ε_a toward lower T in finite H_b is similar to that at $H=0$. At $H=0, \varepsilon_a$ decreases in a stepwise fashion upon increasing T from 2 K, and seems to have two transitions (at ~5 and ~8 K) below 10 K. The application of H_b appears to suppress the lower-T transition and reduces the hysteresis region around T_N(Gd) and the magnitude of ε_a in the ground state. The anomaly around T_N(Gd) gradually shifts toward higher T with increasing H_b.

The most striking magnetic-field effect on ε of $GdMnO_3$ was for H applied along *c*. As seen in Figs. 13(c) and 13(f), the application of H_c also shifts the dielectric anomaly at T_{lock} toward higher T as was observed for H_a and H_b. However, the temperature of the anomaly, i.e., T_{lock}, more rapidly increases with increasing H_c ($T_{\text{lock}} \sim 33$ K at 9 T). In addition, the application of H_c significantly enhances the magnitude of ε_c below T_{lock}. The anomaly around T_N(Gd) is extinguished by applying H_c, as well as H_a.

We also investigated the effect of applying H_b on P. In $GdMnO_3$, a finite P was observed only for the configuration with P along the *a* axis and H along the *b* axis in magnetic fields below 9 T. In Fig. 14, we display the T dependence of the polarization for a range of magnetic fields in this configuration. To begin with, let us explain the data at $H=0$. In the previous paper,[12] we mentioned that $GdMnO_3$ is basically paraelectric in the absence of magnetic fields. This was because $GdMnO_3$ does not show remarkable spontaneous polarization as $TbMnO_3$ and $DyMnO_3$. Here, we present more detailed data, which indicate that electric property of $GdMnO_3$ is rather complicated. Two different P–T data at $H=0$ are shown in Fig. 14 (black and red dots). For the P–T data denoted by black dots ($0T\_A$), the poling electric field was always applied during the measurements. The data denoted by red dots ($0T\_B$) were taken by the normal procedure, in which electric fields were removed before measurements. However, the poling was done only down to 6.5 K. The $0T\_A$ data shows a bump structure at temperatures be-

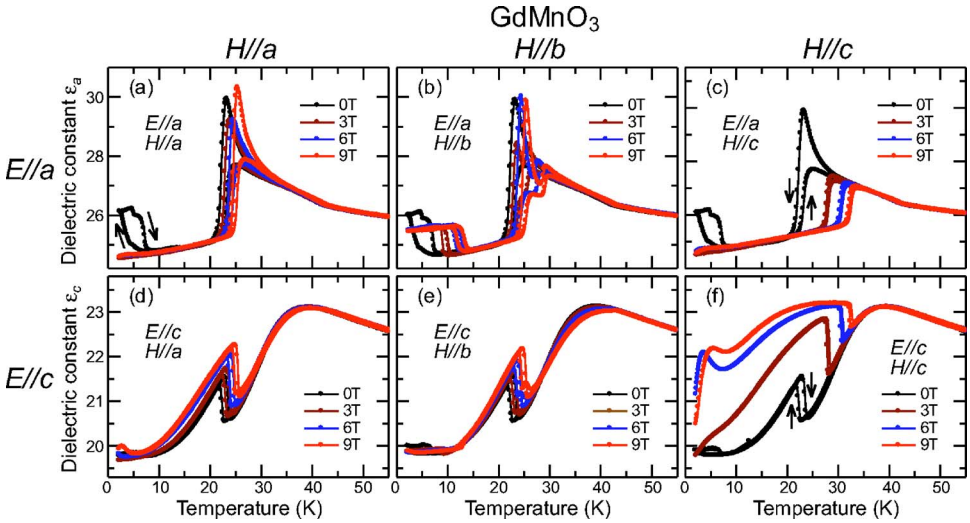

FIG. 13. (Color online) Temperature profiles of dielectric constant along the *a* and *c* axes at various magnetic fields (up to 9 T) along the *a*, *b*, and *c* axes for $GdMnO_3$ crystals.

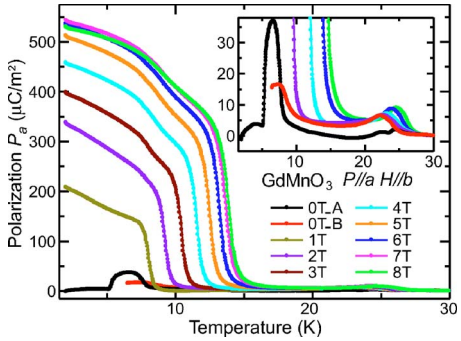

FIG. 14. (Color online) Temperature profiles of electric polarization along the a axis at various magnetic fields (up to 8 T) along the b axis for a $GdMnO_3$ crystal. Except for the data denoted by black dots ($0T\_A$), all the data were taken at zero electric fields after poling the crystal. The measurements for the $0T\_A$ data (black) were done while always applying an electric field (~200 V/mm). The inset shows a magnified view.

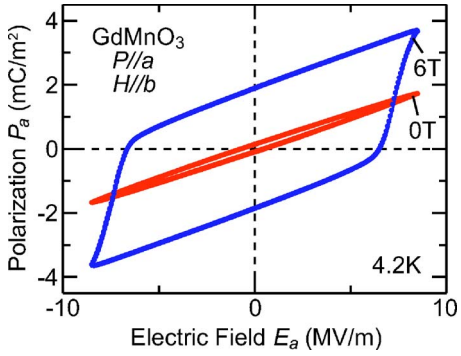

FIG. 15. (Color online) P–E curves obtained at magnetic fields of 0 T (red) and 6 T (blue) for a $GdMnO_3$ crystal. The measurements were done at 4.2 K and 10 Hz. Magnetic and electric fields are applied along the b and a axes, respectively.

tween $T_N(\mathrm{Gd}) \sim 5.1$ K and $T_{C3} \sim 8.2$ K. The feature can be reversed by sign change of electric fields. This result suggests that $GdMnO_3$ shows ferroelectric order with P along the a axis at $T_N(\mathrm{Gd}) < T < T_{C3}$ although the maximum value of $P(\sim 40\ \mu\mathrm{C/m^2})$ is by more than an order of magnitude smaller than those in $TbMnO_3$ and $DyMnO_3$.

It is also worth mentioning that the small spontaneous polarization disappears below $T_N(\mathrm{Gd})$. This is related to the reason why we poled the crystal only down to 6.5 K, i.e., ferroelectric phase, for the measurements of $0T\_B$ data. If the poling electric field is removed below $T_N(\mathrm{Gd})$, namely at nonferroelectric phase, ferroelectric single-domain state cannot be realized during the measurement. One of the most intriguing features in the $0T\_B$ data is that weak polarization persists at higher temperatures and disappears around $T_{\mathrm{lock}} \sim 23$ K (the inset of Fig. 14). Since $GdMnO_3$ is located near the phase boundary between the A-type AF and the long-wavelength nearly-lock-in AF phases in the magnetic phase diagram[12] shown in Fig. 1, it is possible to consider that the observed weak polarization is attributed to a minor long-wavelength nearly-lock-in AF phase included in the sample.

The low-T nonferroelectric phase below $T_N(\mathrm{Gd})$ survives at $H_b < \sim 1$ T, but the application of H_b above ~1 T suppresses the phase and makes the ground state ferroelectric. That feature is clearly seen in the 4.2 K P–E curves displayed in Fig. 15 where the data were taken with the $E \| a$ and $H \| b$ configuration at $H=0$ and 6 T. With increasing H_b, both T_{C3} and P_b gradually increase with T_{C3} reaching ~14 K above ~7 T. As seen in the inset of Fig. 14, the anomaly in P around T_{lock} shifts toward higher temperatures with increasing H, the feature which is in accordance with the anomaly in ε [Figs. 13(b) and 13(e)]. The close relationship between magnetism and the induced ferroelectricity can be seen in the comparison between M–H and P–H curves at fixed temperatures (Fig. 16). Metamagnetic features are also observed in M–H curves at the onset field of the field-induced ferroelectric order.

In Fig. 17, we summarize the results of $GdMnO_3$ by showing the magnetoelectric phase diagrams. (In the phase diagrams, we do not classify the phase showing weak spontaneous polarization at $T_{C3} < T < T_{\mathrm{lock}}$ as ferroelectric.) Unlike $TbMnO_3$ and $DyMnO_3$, the ground state of $GdMnO_3$ is not ferroelectric in the absence of magnetic fields. However, ferroelectric order can be induced by the application of a rather low magnetic field ($< \sim 1$ T) along the b axis [Fig. 16(b)]. The ferroelectric phase with P along the a axis induced by H_b is identical with those in $TbMnO_3$ and $DyMnO_3$ [compare Fig. 17(b) with Figs. 7(b) and 12(b)]. The weak but complex ferroelectric behavior of $GdMnO_3$ can be a result of where $GdMnO_3$ sits in the magnetic phase diagram of $RMnO_3$.

IV. DISCUSSION

A. Electric polarization flop by applying magnetic fields along the a and b axes in $TbMnO_3$ and $DyMnO_3$

To understand the mechanism responsible for switching of the polarization direction with magnetic fields along the a

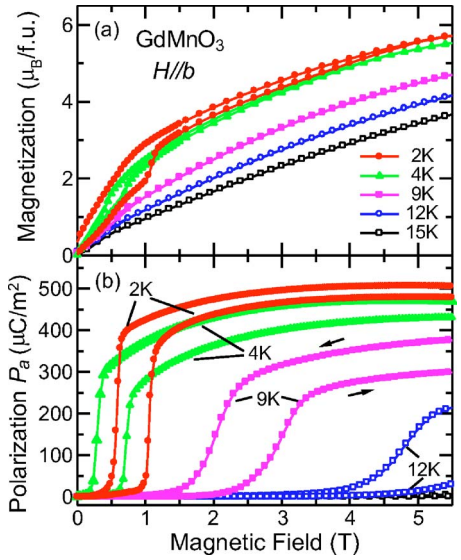

FIG. 16. (Color online) (a) magnetization and (b) magnetic-field-induced change in electric polarization along the a axis for $GdMnO_3$ crystals as a function of an external magnetic field parallel to the b axis at fixed temperatures.

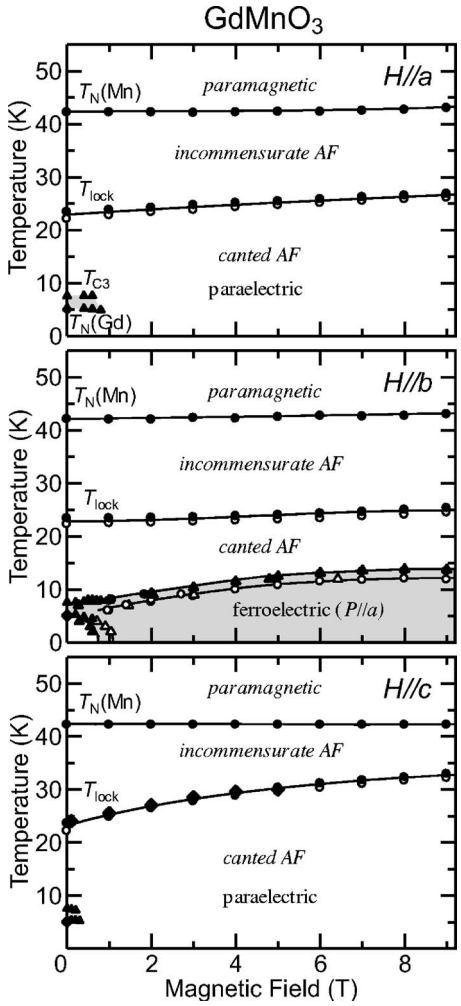

FIG. 17. Magnetoelectric phase diagram of $GdMnO_3$ with magnetic field along the *a* (a), *b* (b), and *c* (c) axes. Circles, triangles, and diamonds represent the data obtained by measurements of dielectric constant, pyroelectric (or magnetoelectric) current, and magnetization, respectively. Open and closed symbols denote the data obtained with decreasing temperature (or increasing a magnetic field) and increasing temperature (or decreasing a magnetic field), respectively. Gray regions indicate ferroelectric phases.

and *b* axes in $TbMnO_3$ and $DyMnO_3$, we need to examine the metamagnetic transitions which accompany abrupt change in electric polarization [Figs. 6(a) and 6(b)]. Since there are no published results on the magnetic structures of these rare-earth manganites in an external magnetic field, we infer these structures from the results of other orthorhombic terbium perovskites. Similar metamagnetic transitions also show up in $TbFeO_3$,[29,30] in which the metamagnetic transitions for *H* along the *a* and the *b* axis have been interpreted as the magnetic reversal of Ising Tb moments. In $TbFeO_3$, the Tb ions occupy four inequivalent positions, and are polarized along two Ising axes within the *ab* plane at $\theta=54°$ from the *b* axis. The magnetic configuration of Tb sites in $TbFeO_3$ below T_N(Tb) were given as the type A_xG_y in Bertaut's notation[31] (the irreducible representation Γ_8 of the space group $D_{2h}^{16}-Pbnm$) [Figs. 18(a) and 18(b)]. With *H* along the *a* axis in $TbFeO_3$, a single transition occurs at

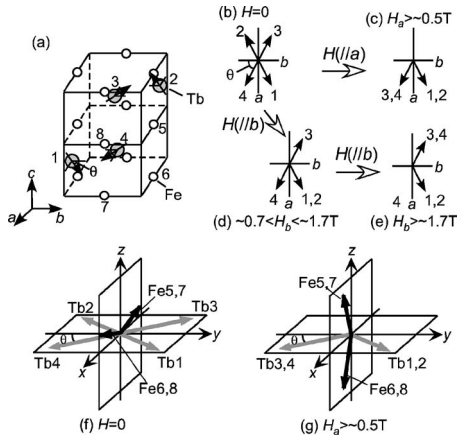

FIG. 18. (a) Schematic magnetic configurations at $H=0$ on Tb ions in $TbFeO_3$. (b)–(e) Evolution of Tb moment arrangements projected for the *ab* plane by applying magnetic fields along the *a* and *b* axes in $TbFeO_3$. (f) and (g) Spin reversal of Tb moments and spin reorientation of Fe moments by applying magnetic fields along the *a* axis in $TbFeO_3$.

$\sim$0.5 T as Tb moments at two of the sites, say the sites 2 and 3, are reversed (the type F_xC_y) [Fig. 18(c)]. With *H* along the *b* axis in $TbFeO_3$, the moment reversal occurs in two stages. First, the moments at one of Tb sites, say the site 2, becomes reversed at $\sim$0.7 T [Fig. 18(d)]. Then the moment at the site 4 is reversed at $\sim$1.7 T (the type C_xF_y) [Fig. 18(e)]. In coincidence with the spin reversal of Tb moments in $TbFeO_3$, there occur spin-reorientation transitions in the Fe moments, as shown in Figs. 18(f) [for $H=0$] and 18(g) [for $H_a>\sim0.5$ T].

In the case of $TbMnO_3$ investigated in the present work, the ordered structure of Tb moments having long wavelength AF order with the wave vector $(0,\sim0.42,1)$ at $H=0$ is different from that in $TbFeO_3$ as illustrated in Fig. 18(a). However, the Tb moments in $TbMnO_3$ similarly lie along two Ising directions with respect to the *b* axis ($\theta=57°$) within the *ab* plane[23] as in $TbFeO_3$. As mentioned above, little work has been done on the spin structures in $TbMnO_3$ under applied magnetic fields. However, metamagnetic features similar to those observed in $TbFeO_3$ suggest the similar reversal process of the Tb moments and spin reorientation of Mn moments by applying *H* along the *a* and *b* axes.

In the previous paper,[12] we discussed the importance of lattice modulation with nonzero wave vector for ferroelectricity in $TbMnO_3$ and $DyMnO_3$, as in conventional improper ferroelectrics.[32,33] The lattice modulation in these manganites can be regarded as a second harmonic that is magnetoelastically induced by long wavelength AF order, and can break the spatial inversion symmetry. To understand why the spontaneous polarization appears along the *c* axis, we need to analyze symmetry of the modulated magnetic and crystallographic structure. However, the detailed magnetic and crystallographic structures of the ferroelectric phase of $TbMnO_3$ have not been solved even for $H=0$ mainly because of their complexity such as the long wavelength magnetic structure and the existence of multiple magnetic components.[24]

At present, we speculate that the electric polarization flop produced by applying *H* along the *a* or *b* axis is related to the

change of the wave number k_l at the Tb spin reversal. There are several examples that show an electric polarization flop accompanying the change of a wave number for lattice modulation. $[N(CH_3)_4]_2ZnCl_4$ (Ref. 34) and $(CH_3)_3NCH_2COO\cdot CaCl_2\cdot 2H_2O$ (Ref. 35) (BCCD) are dielectric compounds that show an incomplete devil's staircase where a wave number for lattice modulation changes in a stepwise shape with varying T.[36] In these compounds, numerous long wavelength commensurate phases with different modulation wave numbers appear with changing T. (Here, *commensurate* phase means the phase in which the modulation wave vector can be represented as the quotient n/m of two integers.) The direction or magnitude of polarization changes with the variation of the modulation wave number. For instance, in BCCD having the fundamental space group *Pbnm*, the commensurate phases with modulation wave vector $(\delta,0,0)[\delta=1/4,2/9,1/5,\ldots]$ exhibit polarizations along the b and c axes, and zero polarization, …, respectively.[37,38] By means of a symmetry analysis, Perez-Mato[35] explains the successive changes in the polarity of BCCD, and predicts that the polarity of a modulated commensurate phase having wave number $\delta=n/m$ (n and m; integers) depends on the parity of the function δ, i.e., whether n and m are even or odd, as well as on the phase angle of the modulation relative to the unit cell. Such an approach may also be applied to the field-induced electric polarization flop in RMnO$_3$ (R=Tb and Dy).

The spin reversal and/or spin reorientation generally involve a change in magnetic symmetry as well as irreducible representation, as spin flop transitions where sudden change of the direction of magnetoelectrically induced polarization has been observed in several conventional magnetoelectrics.[2,10] It is possible to consider that the variation of magnetic symmetry brings about the change in wave vector of lattice modulation which is tied with crystallographic symmetry so as to remove the discrepancy between the direction of electric polarization determined by magnetic symmetry and that by crystallographic one. Considering the strong interplay of lattice modulation and magnetic order, which is described by the relation of $k_l=2k_s$ (k_s: modulation wave number of magnetic order), the spin reversal and/or spin reorientation may also act on the magnetic modulation as well as the lattice one. Thus, we can speculate that the spin reversal and/or spin reorientation trigger sudden changes of electric polarization such as the electric polarization flop in RMnO$_3$ (R=Tb and Dy). Furthermore, it is also possible to infer that the lock-in transition at $T_{\rm lock}(=T_C)$ is ascribed to a change of magnetic symmetry which is suggested by the appearance of the G-, C-, and F-type components at $T_{\rm lock}$ in TbMnO$_3$.[24] However, further detailed investigations of the crystallographic and magnetic lattice structures are needed to test this suggestion.

B. Disappearance of ferroelectricity by applying a magnetic field along the c axis in TbMnO$_3$

As shown in Fig. 7(c), ferroelectric order vanishes in TbMnO$_3$ when high magnetic fields are applied along the c axis. Here, we discuss a possible origin of this field-induced disappearance of ferroelectricity. Let us begin with a systematic discussion of the magnetic properties for perovskite rare-earth manganites. Figure 19 displays the T profiles of M at selected H applied along the c axis for RMnO$_3$ (R=Gd, Tb, and Dy). In GdMnO$_3$ [Fig. 19(a)], M shows a sudden jump ($\Delta M\sim 0.2\mu_B$/f.u.) at ~24 K and 0.1 T. The temperature corresponds to $T_{\rm lock}$ where the system undergoes a transition from a sinusoidal AF to canted A-type AF order for the Mn moments.[20,28] Such a sudden jump of M at $T_{\rm lock}$ was not observed with H along the a and the b axes (not shown). These results indicate that the canting moment ($\sim 0.2\mu_B$/Mn site) is along the c axis, which coincides with the case of a typical A-type AF LaMnO$_3$.[39] The origin of the canting moment along the c axis in the A-type AF LaMnO$_3$ has been discussed in terms of the Dzyaloshinskii–Moriya interaction.[39,40] With increasing H_c, the magnetization jump shifts monotonically toward higher T. This shift can be understood in terms of the stabilization of the A-type AF state with the canting moment along the c axis by applying H_c. If we compare the magnetization data with the corresponding dielectric constant data, we find that the sudden jump of M accompanies that of ε [Figs. 13(c) and 13(f)].

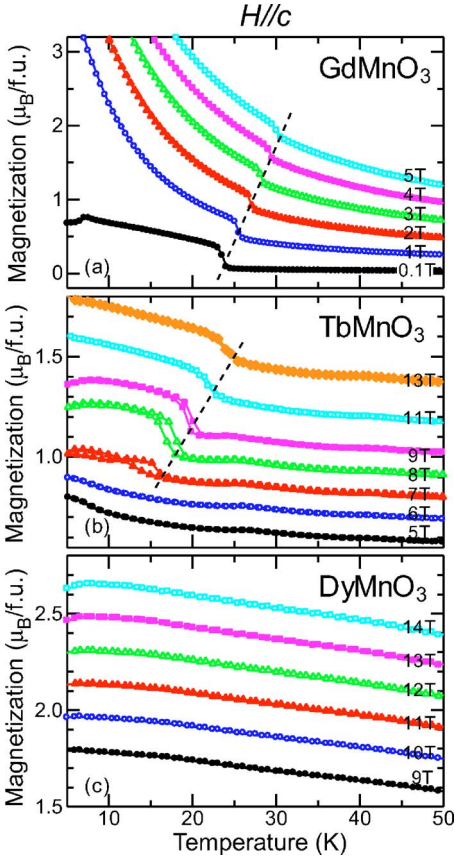

FIG. 19. (Color online) Temperature profiles of magnetization at various magnetic fields for crystals of (a) GdMnO$_3$, (b) TbMnO$_3$, and (c) DyMnO$_3$. Steep increases of magnetization around dotted lines denote the onset of the canted A-type AF order.

As seen in Fig. 19(b), no special features are observed in M below 6 T for TbMnO$_3$. However, some increase of M at ~16 K can be seen in 7 T data, and a steep increase of M ($\sim 0.2\mu_B$/Mn site) can be observed above 8 T. As in

$GdMnO_3$, the steep increase of M is shifted toward higher T with increasing H_c. By analogy with $GdMnO_3$, the steep increase of M may signal the onset canted A-type AF order. This means that the ground state of $TbMnO_3$ becomes A-type AF at high H_c. In fact, this magnetization increase corresponds to the metamagnetic transition shown in Fig. 6(c). From the comparison between magnetic and ferroelectric properties, we can conclude that the disappearance of ferroelectricity with application of H_c in $TbMnO_3$ is attributed to the transition to a canted A-type AF state ($k_{Mn}=0$) which cannot support a lattice modulation with nonzero vector. Moreover, the T profiles of ε_a and ε_c at high H for $TbMnO_3$ [Figs. 5(c) and 4(c)] bear close resemblance to those at low H for $GdMnO_3$ [Figs. 13(c) and 13(f)] as regards a sharp peak structure at T_{lock} in ε_a and enhancement of ε_c below T_{lock}.

Applying H_c will shift the magnetic phase diagram shown in Fig. 1. This magnetic field may expand the A-type AF phase region and shift the boundary between the A-type AF and the ferroelectric long-wavelength commensurate AF phases to right side (see Fig. 1). As clearly seen in Fig. 1, $DyMnO_3$ is located far from this phase boundary. This is the reason why the canted AF phase has not been observed in $DyMnO_3$ at magnetic fields up to 14 T [Fig. 12(c)], but we expect that still higher magnetic fields may induce the A-type AF phase and suppress the ferroelectric phase in $DyMnO_3$ as well.

V. SUMMARY

We have investigated magnetic-field effect on magnetic, dielectric, and ferroelectric properties for single crystals of $RMnO_3$ (R= Gd, Tb, and Dy) with orthorhombically distorted perovskite structure. Magnetoelectric phase diagrams of these orthorhombic rare-earth manganites have been determined from measurements of magnetization, dielectric constant, and electric polarization for magnetic fields along different crystallographic directions. Our systematic investigation shows that several types of metamagnetic transitions [e.g., the reversal of R f-electron moments, transition from long wavelength antiferromagnetic to layered-type (A-type) antiferromagnetic states of Mn d-electron moments] produce the magnetic-field-induced changes in dielectric and ferroelectric properties. In these rare-earth manganites, we can either induce or suppress ferroelectric order by applying a magnetic field. In addition, we can switch the direction of the ferroelectric polarization vector by using a magnetic field. A variety of magnetic-field induced magnetoelectric phase transitions are realized by fine tuning of the subtle balance of competing magnetic interactions that produce complex modulated magnetic structures with long wavelength. The results presented here indicate that magnetic insulators with long-wavelength magnetic structures provide a route to design of magnetoelectric multiferroics showing gigantic magnetoelectric phenomena.

ACKNOWLEDGMENTS

We thank T. Arima, R. Kajimoto, D. N. Argyriou, N. Aliouane, S. Murakami, and N. Nagaosa for helpful discussions, and K. J. McClellan, J. C. Lashley, F. R. Drymiotis, H. Shintani, A. Sawa, S. Horiuchi, and J. L. Sarrao for help with experiments. This work was in part supported by U.S. Department of Energy and Grant-in-Aids for Scientific Research from the MEXT, Japan.

*Present address: Department of Physics and Astronomy, Wayne State University, Detroit, MI 48201, USA.

[1] G. A. Smolenskii and I. E. Chupis, Usp. Fiz. Nauk **137**, 415 (1982); also Sov. Phys. Usp. **25**, 475 (1982).
[2] *Magnetoelectric Interaction Phenomena in Crystals*, edited by A. J. Freeman and H. Schmid (Gordon and Breach, London, 1975).
[3] Z. J. Huang, Y. Cao, Y. Y. Sun, Y. Y. Xue, and C. W. Chu, Phys. Rev. B **56**, 2623 (1997).
[4] N. A. Hill, J. Phys. Chem. B **104**, 6694 (2000).
[5] M. Fiebig, Th. Lottermoser, D. Frohlich, A. V. Goltsev, and R. V. Pisarev, Nature (London) **419**, 818 (2001).
[6] J. Wang, J. B. Neaton, H. Zheng, V. Nagarajan, S. B. Ogale, B. Liu, D. Viehland, V. Vaithyanathan, D. G. Schlom, U. V. Waghmare, N. A. Spaldin, K. M. Rabe, M. Wutting, and R. Ramesh, Science **299**, 1719 (2003).
[7] T. Kimura, S. Kawamoto, I. Yamada, M. Azuma, M. Takano, and Y. Tokura, Phys. Rev. B **67**, 180401(R) (2003).
[8] H. Schmid, Ferroelectrics **62**, 317 (1994).
[9] H. Schmid, Ferroelectrics **221**, 9 (1999).
[10] H. Schmid, Magnetoelectric Effects in Insulationg Magnetic Materials, in *Introduction to Complex Mediums for Optics and Electromagnetics*, edited by W. S. Weiglhoger and A. Lakhtakia (SPIE Press, Bellingham, WA, 2003), p. 167.
[11] T. Kimura, T. Goto, H. Shintani, K. Ishizaka, T. Arima, and Y. Tokura, Nature (London) **426**, 55 (2003).
[12] T. Goto, T. Kimura, G. Lawes, A. P. Ramirez, and Y. Tokura, Phys. Rev. Lett. **92**, 257201 (2004).
[13] K. Saito and K. Kohn, J. Phys.: Condens. Matter **7**, 2855 (1995).
[14] H. Nakamura and K. Kohn, Ferroelectrics **204**, 107 (1997).
[15] Y. Koyama, H. Nakamura, N. Iwata, A. Inomata, and K. Kohn, J. Phys. Soc. Jpn. **65**, 1383 (1996).
[16] Y. F. Popov, A. M. Kadomtseva, G. P. Vorobév, S. S. Krotov, K. I. Kamilov, and M. M. Lukina, Phys. Solid State **45**, 2155 (2003).
[17] N. Hur, S. Park, P. A. Sharma, J. S. Ahn, S. Guha, and S.-W. Cheong, Nature (London) **429**, 392 (2004).
[18] S. Kobayashi, T. Osawa, H. Kimura, Y. Noda, I. Kagomiya, and K. Kohn, J. Phys. Soc. Jpn. **73**, 1593 (2004).
[19] D. Higashiyama, S. Miyasaka, N. Kida, T. Arima, and Y. Tokura, Phys. Rev. B **70**, 174405 (2004).
[20] T. Kimura, S. Ishihara, H. Shintani, T. Arima, K. T. Takahashi, K. Ishizaka, and Y. Tokura, Phys. Rev. B **68**, 060403(R) (2003).
[21] D. Shannon, Acta Crystallogr. **A32**, 751 (1976).
[22] T. Mori, K. Aoki, N. Kamegashira, T. Shishido, and T. Fukuda, Mater. Lett. **42**, 387 (2000).
[23] S. Quezel, F. Tcheou, J. Rossat-Mignod, G. Quezel, and E.

Roudaut, Physica B & C **86–88B**, 916 (1977).
[24] R. Kajimoto, H. Yoshizawa, H. Shintani, T. Kimura, and Y. Tokura, Phys. Rev. B **70**, 012401 (2004); **70**, 219904 (E) (2004).
[25] Different batch crystals were used for the measurements at high magnetic fields, which is the reason for slightly discrepancies in the magnitude of ε and P between the data of Figs. 2 and 3, and Figs. 4 and 5.
[26] In Figs. 4(d) and 4(e), P_c is still finite even at 14 T. But this may be caused by P_a component due to some misalignment of sample axes.
[27] We also measured the P–E curves with the $E \| c$ configuration where we can expect that the ferroelectric hysteresis loop appears at 0 T. However, coercive field appears to be high in this configuration. Then, the crystal showed dielectric breakdown before forming a clear hysteresis loop.
[28] J. Hemberger, S. Lobina, H.-A. Krug von Nidda, N. Tristan, V. Y. Ivanov, A. A. Mukhim, A. M. Balbashov, and A. Loidl, Phys. Rev. B **70**, 024414 (2004).
[29] J. E. Bouree and J. Hammann, J. Phys. (Paris) **36**, 391 (1975).
[30] R. Bidaux, J. E. Bouree, and J. Hammann, J. Phys. (Paris) **36**, 803 (1975).
[31] E. F. Bertaut, in *Magnetism III*, edited by G. T. Rado and H. Suhl (Academic Press, New York, 1963), p. 149.
[32] A. P. Levenyuk and D. G. Shannikov, Usp. Fiz. Nauk **112**, 561 (1974); also Sov. Phys. Usp. **17**, 199 (1974).
[33] R. Blinc and A. P. Levanyuk, *Incommensurate Phases in Dielectrics* (North-Holland, Amsterdam, 1986).
[34] H. Mashiyama, J. Phys. Soc. Jpn. **49**, 2270 (1980).
[35] J. M. Perez-Mato, Solid State Commun. **67**, 1145 (1988).
[36] P. Bak, Rep. Prog. Phys. **45**, 587 (1982).
[37] W. Brill, W. Schildkamp, and J. Spilker, Z. Kristallogr. **172**, 281 (1985); W. Brill and K. H. Ehses, Jpn. J. Appl. Phys., Suppl. **24**, Suppl. 24-2, 826 (1986).
[38] H.-G. Unruh, F. Hero, and V. Dvorak, Solid State Commun. **70**, 403 (1989).
[39] V. Skumryev, F. Ott, J. M. D. Coey, A. Anane, J. P. Renard, L. Pinsard-Gaudart, and A. Revcolevschi, Eur. Phys. J. B **11**, 401 (1999).
[40] I. Solovyev, N. Hamada, and K. Terakura, Phys. Rev. Lett. **76**, 4825 (1996).